

Synthesis, Characterization, and Nanomaterials Generated from 6,6'-(((2-Hydroxyethyl)azanediyl)bis(methylene))bis(2,4-di-*tert*-butylphenol) Modified Group 4 Metal Alkoxides

Timothy J. Boyle,^{*,‡,§} Joshua Farrell,[†] Daniel T. Yonemoto,^{‡,¶} Jeremiah M. Sears,[‡] Jessica M. Rimsza,[§] Diana Perales,[‡] Nelson S. Bell,[‡] Roger E. Cramer,^{||} LaRico J. Treadwell,[‡] Peter Renehan,[†] Casey J. Adams,^{‡,⊥} Michael T. Bender,^{‡,▽} and William Crowley[†]

[‡]Advanced Materials Laboratory, Sandia National Laboratories, 1001 University Boulevard, SE, Albuquerque, New Mexico 87106, United States

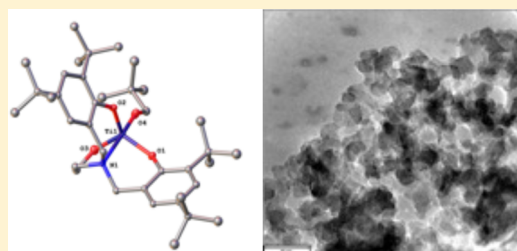
[†]Department of Chemistry, College of the Holy Cross, Box C, 1 College Street, Worcester, Massachusetts 01610, United States

[§]Geochemistry Department, Sandia National Laboratories, PO Box 5800, MS 0754, Albuquerque, New Mexico 87185-0754, United States

^{||}Department of Chemistry, University of Hawaii - Manoa, 2545 McCarthy Mall, Honolulu, Hawaii 96822-2275, United States

Supporting Information

ABSTRACT: The impact on the morphology nanoceramic materials generated from group 4 metal alkoxides ($[M(OR)_4]$) and the same precursors modified by 6,6'-(((2-hydroxyethyl)azanediyl)bis(methylene))bis(2,4-di-*tert*-butylphenol) (referred to as H₃-AM-DBP₂ (1)) was explored. The products isolated from the 1:1 stoichiometric reaction of a series of $[M(OR)_4]$ where M = Ti, Zr, or Hf; OR = OCH(CH₃)₂(OPr^{*t*}); OC(CH₃)₃(OBu^{*t*}); OCH₂C(CH₃)₃(ONep) with H₃-AM-DBP₂ proved, by single crystal X-ray diffraction, to be [(ONep)Ti(*k*^{*t*}(O,O',O'',N)-AM-DBP₂)] (2), [(OR)M(μ (O)-*k*^{*t*}(O',O'',N)-AM-DBP₂)]₂ [M = Zr: OR = OPr^{*t*}, 3-tol; OBu^{*t*}, 4-tol; ONep, 5-tol; M = Hf: OR = OBu^{*t*}, 6-tol; ONep, 7-tol]. The product from each system led to a tetradentate AM-DBP₂ ligand and retention of a parent alkoxide ligand. For the monomeric Ti derivative (2), the metal was solved in a trigonal bipyramidal geometry, whereas for the Zr (3–5) and Hf (6, 7) derivatives a symmetric dinuclear complex was formed where the ethoxide moiety of the AM-DBP₂ ligand bridges to the other metal center, generating an octahedral geometry. High quality density functional theory level gas-phase electronic structure calculations on compounds 2–7 using Gaussian 09 were used for meaningful time dependent density functional theory calculations in the interpretation of the UV–vis absorbance spectral data on 2–7. Nanoparticles generated from the solvothermal treatment of the ONep/AM-DBP₂ modified compounds (2, 5, 7) in comparison to their parent $[M(ONep)_4]$ were larger and had improved regularity and dispersion of the final ceramic nanomaterials.



INTRODUCTION

Group 4 ceramic nanoparticles (NP) are of interest for a number of applications including orthopedic biomaterials,¹ improved drug delivery,² photocatalysts,^{3–5} jewelry, fire-retardant materials,^{6–8} optical storage devices,⁹ light shutters,¹⁰ refractory material gate oxides in microelectronics,^{2,11–14} and high dielectric materials in DRAM capacitors.^{2,13,15} For electronic applications, controlled deposition of the ceramic NPs in three-dimensional architectures is a growing demand for industrial efforts.^{16,17} Direct-write (DW) methods are considered to be a viable route to produce these complex architectures.¹⁸ For these technologies, a computer controlled stage follows a predesigned pattern, depositing layer upon layer of ink to build the desired component. In order to have useful DW printed components, it is critical to have high quality nanoinks (N-inks), which necessitates controlled uniform nanoparticles. It was, therefore, of interest to generate high

dielectric (*k*) nanomaterials for DW printed materials using the group 4 metal oxides (MO₂ where M = Ti, Zr, Hf). This report discusses the first step in production of high quality N-inks, with the development of precursors that will generate tailored morphological ceramic nanoparticles.

Metal alkoxides ($[M(OR)_4]$) are one of the most widely used precursors to ceramic materials; however, due to uncontrolled hydrolysis and condensation pathways for the standard monodentate ligands, irregular nanoparticles are often generated.^{19–22} Polydentate ligands are frequently used to control the structure/decomposition of the $[M(OR)_4]$ precursors.^{23–25} It was reasoned that multidentate ligands might be useful for production of uniform MO₂ NPs via preferential/directed hydrolysis. Previously, we have inves-

Received: July 9, 2018

tigated tridentate ligands such as tris(hydroxymethyl)ethane (H_3 -THME) and tris(hydroxymethyl)propane (H_3 -THMP).²⁴ For the group 4 derivatives, these ligands formed complex tetramers of the general formula $[\mu_3-(O)(\mu-(O',O''))\text{-THMR}]_2M_4(OR)_{10}$.²⁴

In an effort to generate less encumbered molecules to allow for directionalized hydrolysis favoring more uniform nanomaterials production, ligands that are more flexible and chelate to one metal were of interest. The 6,6'-(((2-hydroxyethyl)-azanediyl)bis(methylene))bis(2,4-di-*tert*-butylphenol) ligand, termed H_3 -AM-DBP₂ (**1**, Figure 1), came to the forefront of

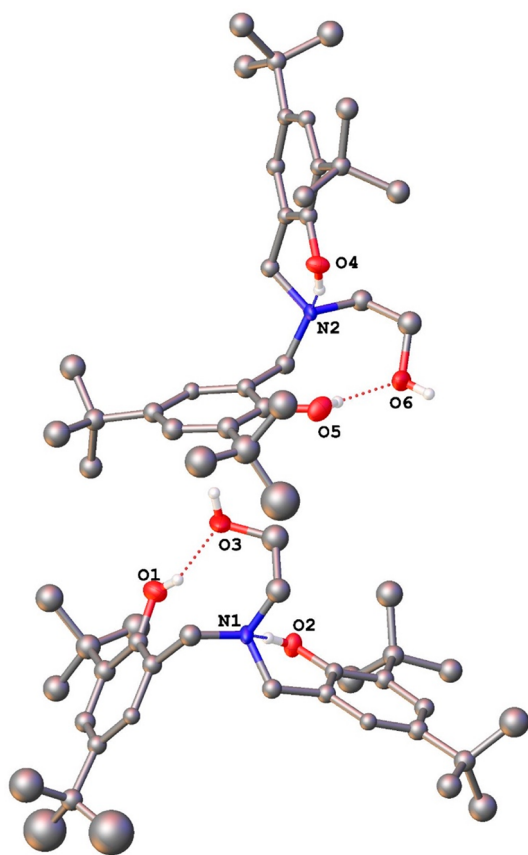
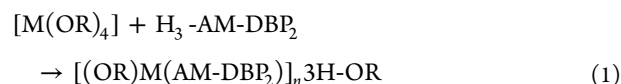


Figure 1. Structure plot of **1**. Thermal ellipsoids of heavy atoms drawn at the 30% level with carbon atoms drawn as ball and stick, and H-atoms are not shown for clarity. See Supporting Information Table S1 for structural parameters.

our efforts due to the steric bulk of the ligand, the multidentate properties, and the flexibility of the ethoxy moiety. The synthesis of this ligand was undertaken following a Mannich reaction pathway,^{26,27} and its coordination behavior with group 4 metals was investigated, according to eq 1. The products isolated proved, by single crystal X-ray experiments, to be H_3 -AM-DBP₂ (**1**), $[(\text{ONep})\text{Ti}(k^4(O,O',O''),N)\text{-AM-DBP}_2)]$ (**2**), $[(\text{OR})\text{M}(\mu(O)-k^3(O',O''),N)\text{-AM-DBP}_2)]_2$ [$M = \text{Zr}$: OR = OPr^i , 3-tol; OBU^f , 4-tol; ONep , 5-tol; $M = \text{Hf}$: OR = OBU^f , 6-tol; ONep , 7-tol where $\text{OPr}^i = \text{OCH}(\text{CH}_3)_2$, $\text{OBU}^f = \text{OC}(\text{CH}_3)_3$, $\text{ONep} = \text{OCH}_2\text{C}(\text{CH}_3)_3$]. Schematic structures of the general coordination of these products are shown in Scheme 1. The synthesis and characterization of **1–7** are reported.



The parent alkoxides $[\text{M}(\text{ONep})_4]_2$ ($M = \text{Ti}$,²⁸ Zr ,²⁹ and Hf ²⁹) and the complementary AM-DBP₂/ONep ligated compounds **2**, **5**, and **7** were used to generate nanomaterials under solvothermal (SOLVO; octadecene) conditions. A comparison of the final materials was undertaken using dynamic light scattering (DLS), transmission electron microscopy (TEM), and powder X-ray diffraction (PXRD) to determine the influence that the AM-DBP₂ ligand has on the thermal properties of the precursor and final materials' properties.

EXPERIMENTAL SECTION

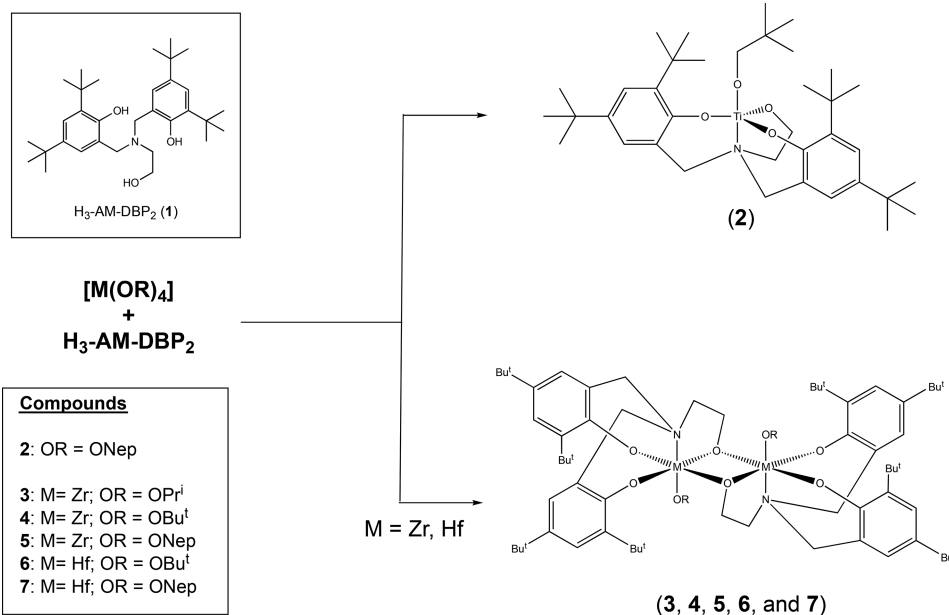
Organic Synthesis. All starting reagents were purchased from commercial sources and used as received. NMR spectra were recorded on an Oxford AS400 spectrometer and referenced to residual peaks in the deuterated solvents.

H_3 -AM-DBP₂ (**1**).³⁰ Following established Mannich condensation-like synthesis routes,^{26,27} ethanolamine (0.61 g, 10 mmol), 2,4-di-*tert*-butylphenol (4.3 g, 21 mmol), and *p*-formaldehyde (0.63 g, 21 mmol) were added to a 48 mL pressure flask equipped with a magnetic stir bar. The flask was sealed, stirred, and heated to 90 °C for 18 h, whereupon the reaction mixture liquefied and then solidified. After cooling, methanol was added to the crude reaction mixture, followed by sonication, filtration, and crystallization, which resulted in the isolation of a pure white powder of **1**. Additional product was obtained from crystallization of the mother liquor. Yield 4.0 g, 81.0%. ¹H NMR (CDCl_3) δ 7.21 (2H, d, $\text{C}_6\text{H}_2(\text{C}(\text{CH}_3)_3)_2\text{OH}$, $J_{\text{H-H}} = 2.4$ Hz), 6.90 (2H, d, $\text{C}_6\text{H}_2(\text{C}(\text{CH}_3)_3)_2\text{OH}$, $J_{\text{H-H}} = 2.4$ Hz), 3.88 (2H, t, $\text{HOCH}_2\text{CH}_2\text{N}$, $J_{\text{H-H}} = 5.2$ Hz), 3.76 (4H, s, PhCH_2N), 2.73 (2H, t, $\text{HOCH}_2\text{CH}_2\text{N}$, $J = 5.2$ Hz), 1.39 (18 H, s, $\text{C}_6\text{H}_2(\text{C}(\text{CH}_3)_3)_2\text{OH}$), 1.27 (18 H, s, $\text{C}_6\text{H}_2(\text{C}(\text{CH}_3)_3)_2\text{OH}$). ¹³C (CDCl_3) δ 152.75 (Ar-C), 141.20 (Ar-C), 136.13 (Ar-C), 125.12 (Ar-C), 123.67 (Ar-C), 121.68 (Ar-C), 61.15 ($\text{NCH}_2\text{CH}_2\text{OH}$), 57.81 (ArCH₂N), 53.56 ($\text{NCH}_2\text{CH}_2\text{OH}$), 35.03 (Ar-C(CH₃)₃), 34.26 (Ar-C(CH₃)₃), 31.80 (Ar-C(CH₃)₃), 29.75 (Ar-C(CH₃)₃). X-ray-quality crystals were obtained by slow evaporation of a MeOH solution, resulting in the formation of clear and colorless plates over the course of 4 days.

Inorganic Synthesis. All compounds and reactions described below were handled with rigorous exclusion of air and water using standard Schlenk line and argon filled glovebox techniques. All solvents were stored under argon and used as received in (Aldrich) Sure/Seal bottles, including hexane, toluene, tetrahydrofuran, pyridine (solv). The following chemicals were used as received (Aldrich and Alfa Aesar): titanium isopropoxide ($[\text{Ti}(\text{OPr}^i)_4]$), titanium *tert*-butoxide ($[\text{Ti}(\text{OBU}^f)_4]$), zirconium isopropoxide complex ($[\text{Zr}(\text{OPr}^i)_4\text{HOPr}^i]_2$), zirconium *tert*-butoxide ($[\text{Zr}(\text{OBU}^f)_4]$), hafnium *tert*-butoxide ($[\text{Hf}(\text{OBU}^f)_4]$), and *neo*-pentanol (H-ONep). The following compounds were prepared according to literature procedures: $[\text{Ti}(\mu\text{-ONep})(\text{ONep})_3]_2$,²⁸ $[\text{M}(\mu\text{-ONep})_2(\mu\text{-OBU}^f)(\text{ONep})_6]_2$ ($M = \text{Zr}$, Hf)²⁹ (Note: these compounds are referred to as $[\text{M}(\text{ONep})_4]$ throughout the paper for simplicity). $[(\text{OR})\text{Ti}(k^4(O,O',O''),N)\text{-AM-DBP}_2]$ was synthesized according to eq 1 using H_3 -AM-DBP₂ (**1**) and $[\text{Ti}(\text{OR})_4]$ (where OR = OPr^i , OBU^f) and concurrence of both the structure and analytical data with the previously reported characterization data.³¹

All analytical data were collected using dried crystalline material. Fourier-transform infrared (FTIR) spectroscopic data were obtained from a KBr pressed pellet of the sample using a Bruker Vector 22 Instrument under an atmosphere of flowing nitrogen. Elemental analyses were performed on a PerkinElmer 2400 CHN-S/O elemental analyzer.

General Synthesis. In an argon filled glovebox, the off-white powder H_3 -AM-DBP₂ was added to a vial that contained the appropriate $[\text{M}(\text{OR})_4]$ dissolved in toluene. After being stirred for 12

Scheme 1. Schematic Representation of H₃-AM-DBP₂ (1) and Coordination Structures Isolated

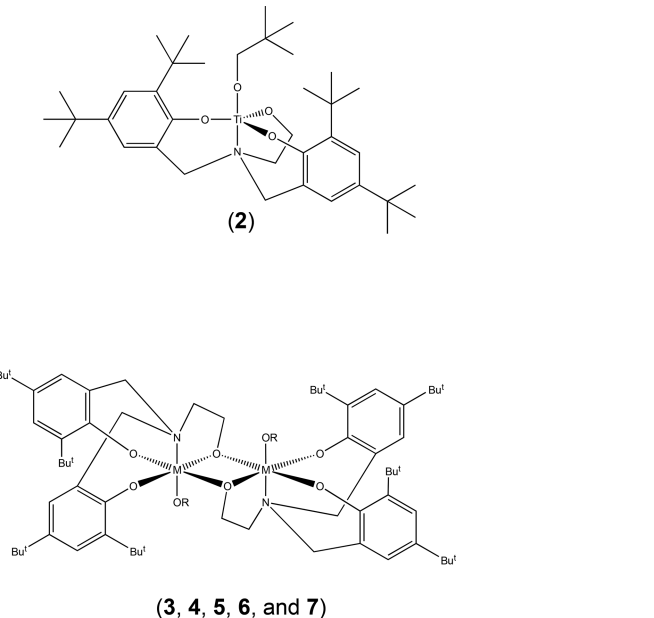
h, the reaction mixture was allowed to sit with the cap removed until X-ray quality crystals formed. The mother liquor was then removed, some crystals were set aside for X-ray studies, and the remainder of the powder were dried *in vacuo* for analytical evaluation. The final yields were not optimized.

[(ONep)Ti($k^4(O',O'',N)$ -AM-DBP₂)] (2). Used [Ti(ONep)₄] (0.500 g, 1.26 mmol) and H₃-AM-DBP₂ (0.628 g, 1.26 mmol) in toluene (5 mL) turned a pale orange-yellow color. Yield 98.0% (0.778 g). FTIR (KBr, cm⁻¹) 2953(s), 2901(m), 2867(m), 1604(w), 1477(s), 1442(s), 1414(m), 1389(w), 1360(m), 1308(m), 1295(w), 1256(s), 1243(s), 1189(s), 1172(s), 1129(m), 1107(m), 1076(s), 1029(s), 916(m), 897(w), 877(m), 850(s), 812(w), 792(m), 759(s), 610(s), 596(s), 584(s), 494(m). Elemental Analyses calc'd for C₃₇H₅₉NO₄Ti (MW = 629.75, 2): 70.57% C; 9.44% H; 2.22% N. Found 70.49% C; 9.72% H; 2.22% N.

[(OPri^t)Zr($\mu(O)-k^3(O',O'',N)$ -AM-DBP₂)]₂ (3)·tol. Used [Zr(OPri^t)₄·HOPri^t]₂ (0.155 g, 0.401 mmol) and H₃-AM-DBP₂ (0.200 g, 0.401 mmol) in toluene (5 mL). Yield 87.5% (0.258 g). FTIR (KBr, cm⁻¹) 2964(s), 2928(m), 2866(m), 2624(w), 1604(w), 1478(s), 1442(s), 1415(m), 1361(s), 1337(m), 1315(m), 1264(s), 1243(s), 1134(s, br), 1055(m), 1008(s), 947(m), 915(w), 876(m), 844(s), 752(m), 729(w), 602(w), 551(m), 487(w), 462(m). Elemental Analyses calc'd for C₇₇H₁₁₈N₂O₈Zr₂ (MW = 1382.25, 3·tol): 66.91% C; 8.61% H; 2.03% N; C₉₈H₁₄₂N₂O₈Zr₂ (MW = 1658.67, 3·4tol): 70.97% C; 8.63% H; 1.69% N. Found 70.26% C; 9.14% H; 2.07% N.

[(OBU^t)Zr($\mu(O)-k^3(O',O'',N)$ -AM-DBP₂)]₂ (4)·tol. Used [Zr(OBU^t)₄] (0.500 g, 1.30 mmol) and H₃-AM-DBP₂ (0.648 g, 1.30 mmol) in toluene (5 mL). Yield 83.7% (0.870 g). FTIR (KBr, cm⁻¹) 2962(s), 2903(s), 2868(m), 1604(w), 1478(s), 1443(s), 1414(m), 1389(w), 1360(m), 1309(m), 1265(s), 1242(s), 1193(s), 1171(m), 1132(m), 1090(w), 1048(m), 1019(s), 915(w), 875(m), 847(s), 754(m), 548(m), 501(w), 465(m). Elemental Analyses calc'd for C₉₃H₁₃₈N₂O₈Zr₂ (MW = 1594.58; 4·3tol): 70.05% C; 8.72% H; 1.76% N; C₈₆H₁₃₀N₂O₈Zr₂ (MW = 1502.44; 4·2tol): 68.75% C; 8.72% H; 1.86% N. Found 68.42% C; 8.35% H; 1.75% N.

[(ONep)Zr($\mu(O)-k^3(O',O'',N)$ -AM-DBP₂)]₂ (5)·tol. Used [Zr(ONep)₄] (0.200 g, 0.419 mmol) and H₃-AM-DBP₂ (0.208 g, 0.419 mmol) in toluene (~3 mL). Yield 94.7% (0.286 g). FTIR (KBr, cm⁻¹) 2955(s), 2902(s), 2867(s), 1604(w), 1477(s), 1443(s), 1414(m), 1391(w), 1362(m), 1304(m), 1264(s), 1243(s), 1204(m), 1171(m), 1133(m), 1107(m), 1076(m), 1055(w), 974(w), 916(w), 874(m), 843(m), 811(w), 753(m), 729(w), 694(w), 674(w), 637(m), 600(w), 545(m), 518(m), 465(m).



General X-ray Crystal Structure Information. Single crystals were mounted onto a loop from a pool of Fluorolube or Parabar 10312 and immediately placed in a 100 K N₂ vapor stream. X-ray intensities were measured using a Bruker-D8 Venture dual-source diffractometer (Cu K α , λ = 1.5406 Å) and CMOS detector for 1 or a Bruker APEX-II CCD diffractometer with Mo K α radiation (λ = 0.71070 Å) for 2–7. Indexing, frame integration, and structure solutions were performed using the BrukerSHELXTL^{32–34} software package within Apex3³⁴ and/or OLEX2³⁵ suite of software. All final CIF files were checked using the CheckCIF program (<http://www.iucr.org/>). Additional information concerning the data collection and final structural solutions can be found in the Supporting Information or by accessing CIF files through the Cambridge Crystallographic Data Base.³⁶ Additional information concerning the data collection and final structural solutions (Tables S1–S3) of these complexes can be found in the Supporting Information or by accessing CIF files through the Cambridge Crystallographic Data Base. The unit cell parameters for the structurally characterized compounds 1–7 are available in the Supporting Information (Figures S1–S7).

Ultraviolet–visible Absorbance Spectroscopy (UV–vis). UV–vis absorbance spectroscopic data were obtained using a Photonics CCD Array UV–vis spectrophotometer. Samples of H₃-AM-DBP₂ and 2–7 were individually prepared in an argon filled glovebox at a ~0.2 M concentration in toluene. Scans ranged from 200 to 950 nm with a D₂ source and W source with a crossover at 460 nm. See Supporting Information (Figure S8) for UV–vis absorbance spectra of H₃-AM-DBP₂ and 2–7.

Thermogravimetric Analysis (TGA)/Differential Scanning Calorimetry (DSC). The simultaneous TGA/DSC analysis was obtained on a Mettler Toledo model TGA/DSC 1. All experiments were conducted under an argon atmosphere at a heating rate of 10 °C min⁻¹ from room temperature to 1100 °C in an alumina crucible (see Supporting Information Figure S9).

Nanoparticle Synthesis. Upon receipt of octadecene (Sigma-Aldrich, 90% technical grade), the solvent was degassed and then transferred to an argon filled glovebox. Under an inert atmosphere, individual 0.06 M solutions of compounds 2, 5, 7, [Ti(ONep)₄], [Zr(ONep)₄], and [Hf(ONep)₄] in octadecene were produced. A sample of each solution (20 mL) was placed in individual Teflon liners, sealed in a Parr Digestion Bomb, and transferred out of the glovebox. The samples were then placed in a box oven and heated to 180 °C for 24 h, removed, and allowed to cool to room temperature. After this time, the residual was isolated by centrifugation on the benchtop and washed with hexanes (three times). The resulting samples were used without further manipulation.

Dynamic Light Scattering (DLS). Measurement of particle size distribution (PSD) was conducted using a Zetasizer Nano-ZS from Malvern Instruments. Particles were prepared in dilute conditions, by adding 50–100 mg of the nanoparticles to ~5 mL of toluene. Under an argon atmosphere, the samples were then pipetted into the glass cuvettes and capped. Measured samples were of low solid concentration (<10⁻⁴ wt %). Dispersion was promoted by treatment of the suspension in an ultrasonic bath for 2 min (Branson Ultrasonics). Ten measurements of each sample's PSD were performed and examined for particle sedimentation or drift in response with time. The PSD is presented as the average of the 10 measurements (see Supporting Information, Figure S10).

Powder X-ray Diffraction (PXRD). PXRD patterns were obtained using a PANalytical X'Pert Pro diffractometer (10–100° two theta) employing CuK α radiation (1.5406 Å) and a RTMS X'Celerator detector at a scan rate of 0.15°/s for the bulk powders or at a scan rate of 0.15°/s using a zero-background holder. The PXRD patterns were analyzed using JADE 9 software (Materials Data, Inc., Livermore CA) and indexed using The Powder Diffraction File PDF-4+ 2013. Crystallite sizes were determined using Jade v9.6.0. All samples were analyzed using a plastic holder.

Transmission Electron Microscopy (TEM). For TEM analyses, the samples were individually dispersed in toluene and aliquots of the solution placed onto a holey-carbon coated copper TEM grid and allowed to dry prior to analysis. TEM images were obtained by utilizing a JEOL 2100 LaB₆ microscope operated at 200 keV (see Supporting Information, Figure S11).

Computational Modeling. Gas-phase electronic structure calculations were performed on 2–7 using Gaussian 09³⁷ at the density functional theory (DFT) level with the hybrid B3LYP functional (Becke's three parameter hybrid exchange functional with Lee–Yang–Parr correlation function).^{38–40} The LANL2DZ effective core potential basis set^{41,42} was used on the metals (Ti, Zr, and Hf); all other atoms were described using the 6-31G basis set^{43–45} as part of the complete basis set model described by Peterson et al.⁴⁶ The LANL2DZ basis set includes a scalar relativistic correction and has been previously applied to Ti, Zr, and Hf-based molecules resulting in agreement with experimental structures.^{47–50}

Molecular structures were selected from solved crystal structures and optimized in unrestricted calculations (included in Figure S12). All atoms were allowed to relax during optimization. Reasonable agreement in the metrical data between the crystal structures and DFT optimized molecules (Table 1) validates the quality of the DFT models and is discussed in the results. After the initial structural

Table 1. Metrical Data for [(OR)Ti(k⁴(O,O',O''),N)AM-DBP₂]³¹ (*) and 2–10^a

| Distance | M-OR | | M-(μ -OR) | | M---M | |
|----------|--|-------------------------|--|-----------------------|--|-------------|
| | Expt. | Calc'd. | Expt. | Calc'd. | Expt. | Calc'd. |
| * | 1.778(2) | 1.786 | ----- | ----- | ----- | ----- |
| 2 | 1.7849(12) | 1.786 | ----- | 1.848 | ----- | ----- |
| 3 | 1.9337(10) | 1.980 | 2.1586(10) 2.186(1) | 2.177 | 3.5893(4) | 3.659 |
| 4 | 1.9155(18) 1.9211(19) | 1.956(1) | 2.1337(19) 2.2091(19) | 2.215(29) | 3.6174(5) | 3.671 |
| 5 | 1.932(3) | 1.980 | 2.136(3) 2.203 | 2.213(37) | 3.586 | 3.664 |
| 6 | 1.9313(14) | 1.955 | 2.1599(13) 2.1821(13) | 2.190(18) | 3.5976(2) | 3.647 |
| 7 | 1.929(4) | 1.952 | 2.135(4) 2.183 | 2.182(32) | 3.563 | 3.607 |
| | M-N _{AM-DBP2} | | M-O _{AM-DBP2} | | M-O _{AM-EIO} | |
| * | 2.331(3) | 2.378 | 1.841(2) 1.872(2) | 1.854(6) | 1.842(2) | 1.850 |
| 2 | 2.3192(13) | 2.379 | 1.8394(12) 1.8642(11) | 1.855(5) | 1.8391(12) | 1.848 |
| 3 | 2.4348(12) | 2.495 | 1.9915(10) 2.0183(10) | 2.035(1) | 2.1586(10) 2.186(1) | 2.177 |
| 4 | 2.528(2) 2.557(2) | 2.596(3) | 1.9895(18) 1.9942(19) 2.0038(19) 2.005(2) | 2.034(6) | 2.1337(19) 2.2091(19) | 2.215(29) |
| 5 | 2.439(4) | 2.484 | 1.989(3) 2.015(3) | 2.035(1) | 2.136(3) 2.203 | 2.213(37) |
| 6 | 2.3953(17) | 2.445 | 1.9816(13) 2.0107(13) | 2.015(2) | 2.1599(13) 2.1821(13) | 2.190(18) |
| 7 | 2.410(4) | 2.449 | 1.983(4) 2.015(3) | 2.011(2) | 2.135(4) | 2.182(32) |
| | O _{DBP-N-O_{DBP}} | | O _{DBP-N-O_{EIO}} | | RO-M-O _{DBP} | |
| 1 | 76.907 74.993 | ----- | 55.904 94.431 97.915 55.769 | ----- | ----- | ----- |
| * | 68.706 | 67.55 | 71.357 71.374 | 68.81(125) | 98.57(10) 99.64(11) | 101.91(118) |
| 2 | 69.363 | 67.55 | 70.883 71.908 | 71.67(160) | 101.04(5) 98.01(5) | 101.91(118) |
| 3 | 70.491 | 69.61 | 65.272 89.429 | 66.35 88.91 | 90.69(4) 99.63(4) | 96.21(482) |
| 4 | 70.320 70.595 | 69.91(7) | 66.349 66.734 85.346 85.690 | 66.13(3) 86.73(10) | 90.96(8) 91.87(8) 101.28(8) 101.37(8) | 96.86(3.88) |
| 5 | 70.183 | 69.25 | 66.288 88.485 | 66.90 89.28 | 91.25(14) 103.90(14) | 98.04(6.48) |
| 6 | 69.024 | 70.65 | 65.867 91.183 | 65.50(4) 89.94 | 93.26(6) 97.93(6) | 91.4(2) |
| 7 | 70.299 | 68.77 | 66.160 88.826 | 66.64 96.02(5) | 90.68(14) 103.20(14) | 96.02(275) |
| | RO-M-O _{EIO} | | N-M-OR | | M-M-N | |
| * | 98.27(11) | 97.58 | 175.84(11) | 173.07 | ----- | ----- |
| 2 | 97.95(6) | 97.58 | 175.18(5) | 173.07 | ----- | ----- |
| 3 | 89.899 114.08(4) | 89.73 114.26 | 166.04(4) | 167.06 | 88.138 | 87.38 |
| 4 | 86.63(7) 87.52(8) 118.48(8) 118.84(8) | 87.68(14) 119.79(57) | 164.61(8) 165.03(8) | 165.82(24) | 92.34(5) 92.56(5) | 93.60(10) |
| 5 | 91.006 109.95(14) | 100.75(959) | 167.69(13) | 168.08(8) | 86.328 | 85.56 |
| 6 | 92.045 114.12(5) | 94.40(2) 115.27(2) | 169.80(6) | 168.128(2) | 84.410 | 85.79 |
| 7 | 90.775 109.17(16) | 97.26(635) | 168.05(14) | 168.29 | 86.639 | 86.11 |

^aAveraged metrical data are shown without error bars.

relaxations, time dependent density functional theory (TD-DFT) calculations were also performed to identify the energies of the 50 lowest-energy electronic transitions.^{45,51,52} The UV–vis absorbance spectra were then predicted from the calculated electronic transition in the 200–800 nm portion of the spectra using the GaussSum program.⁵³ Plotted individual intensities and the Gaussian interpolations with a full-width-half-max (fwhm) value of 3000 1/cm are included in Supporting Information (Figure S13). The three highest contributions to the UV–vis absorbance spectra and the assigned HOMO → LUMO transitions are included in Table 2.

RESULTS AND DISCUSSION

A search of structurally verified group 4 metals modified by the AM-DBP₂ ligand yielded two compounds: [(OR)Ti(k⁴-

Table 2. Experimental and Calculated (TD-DFT) Adsorption Wavelength, λ (nm), with the Three Primary Contributions (1, 2, 3) and HOMO(H)-LUMO(L) Transitions Assignments

| cmpds | exp't, λ (nm) | calc'd, λ (nm) | individual transitions (nm) | | | | | |
|-------|-----------------------|------------------------|-----------------------------|----------------------------------|------------------|--------------------------------------|-----------------|--------------------------------------|
| | | | first λ | assign. | second λ | assign. | third λ | assign. |
| 2 | 282 | 270 | 291 | H \rightarrow L + 2 | 264 | H-4 \rightarrow L + 1 ^a | 248 | H-5 \rightarrow L + 1 ^a |
| | 330 | 341 | 351 | H \rightarrow L | 343 | H-1 \rightarrow L + 1 | 332 | H-1 \rightarrow L |
| 3 | 298 | 299 | 307 | H-1 \rightarrow L + 1 | 293 | H-2 \rightarrow L ^a | 287 | H-2 \rightarrow L |
| | | | | H \rightarrow L | | | | |
| 4 | 294 | 303 | 310 | H-1 \rightarrow L | 289 | H-2 \rightarrow L | 285 | H-3 \rightarrow L |
| 5 | 294 | 302 | 311 | H \rightarrow L | 294 | H-2 \rightarrow (L, L + 1) | 285 | H-3 \rightarrow L + 2 |
| | | | | H-1 \rightarrow L + 1 | | | | |
| 6 | 293 | 256 | 270 | H \rightarrow L | 254 | H-2 \rightarrow L | 250 | H-1 \rightarrow L + 4 ^a |
| | | | | H-1 \rightarrow L + 1 | | | | |
| 7 | 293 | 267 | 271 | H-9 \rightarrow L ^a | 268 | H-9 \rightarrow L ^a | 255 | H-3 \rightarrow L + 1 ^a |

^aContributes less than 50% of the transition.

(*O,O',O'',N*)AM-DBP₂] where R = OPr^{*i*}, OBU^{*t*}.³¹ It is of note that several other ligands with similar constructs as AM-DBP₂ are available with a fur-2-ylmethyl⁵⁴ or tetrahydrofur-2-yl⁵⁵ moiety replacing the N-CH₂CH₂OH fragment or a methoxide⁵⁶ replacing the N-CH₂CH₂OH. The more complex (ethylenedioxy)diethanamine-based tetraphenoxide ligands, which possess two AM-DBP₂ submoieties linked by -[N-CH₂CH₂-O]₂, have also been used to modify group 4 compounds.^{57,58} The coordination of the metal in the [(OR)Ti(*k*⁴(*O,O',O'',N*)AM-DBP₂)] family of compounds were described as distorted trigonal bipyramidal (TBPY-5) monomers, employing a tetradentate AM-DBP₂ and one parent alkoxide ligand. Similarly, when the 6,6'-(((2-hydroxyethyl)azanediyl)bis(methylene))bis(2,4-dimethylphenol) (H₃-AM-DMP₂), where Me groups replace the Bu^{*t*} groups, was used, monomeric [(OR)Ti(*k*⁴(*O,O',O'',N*)AM-DMP₂)] for OC₆H₃(R')₂-2,6 (where R' = CH₃,⁵⁹ CH(CH₃),⁶⁰ C₆H₅,⁵⁹) and dinuclear [(OR)Ti(μ -(O)(*k*³(*O',O',N*)AM-DMP₂)]₂ for OR = OPr^{*i*},³¹ OBU^{*t*},³¹ OC₆H₄F-2,⁵⁹ and OC₆H₄F₂-2,6, OC₆F₅⁵⁹ compounds were isolated. On the basis of these structure types, it was evident that AM-R₂ (R = DMP or DBP) modified [M(OR)₄] compounds might be useful to induce controlled nanomaterial production. Since the heavier group 4 congeners modified with AM-DBP₂ ligand have not been reported, we undertook their synthesis. Crystal structure parameters and structure plots for 2–7 are available in the Supporting Information. Representative structures are shown in Figures 2, 3, and 4.

Ligand Synthesis. The work by Padmanabhan et al.³¹ reported that the H₃-AM-DBP₂ ligand was synthesized following the Siegl and Chattha³⁰ synthesis. However, access to the original report³⁰ was limited, and the Padmanabhan report³¹ indicated that a complicated crystallization and column purification was necessary to isolate this ligand. To simplify the synthesis of the ligand, the Mannich condensation route was undertaken and found to readily produce H₃-AM-DBP₂ (see Experimental Section). Once isolated, no additional purification was necessary. Because of the limited analytical data previously supplied, full characterization of this compound is presented in the Experimental Section.

A single crystal of 1 was isolated where the two molecules per unit cell clearly show the proposed connectivity. Strong H-bonding was observed in each molecule between one of the phenol and ethanol oxygen atoms (O_{OAr}---H---O_{EtOH}-H: O(6)---H(5) = 1.999 Å; O(3)---H(1) = 2.040 Å). An additional weak H-bond interaction of H(1) and H(5) atoms with their parent

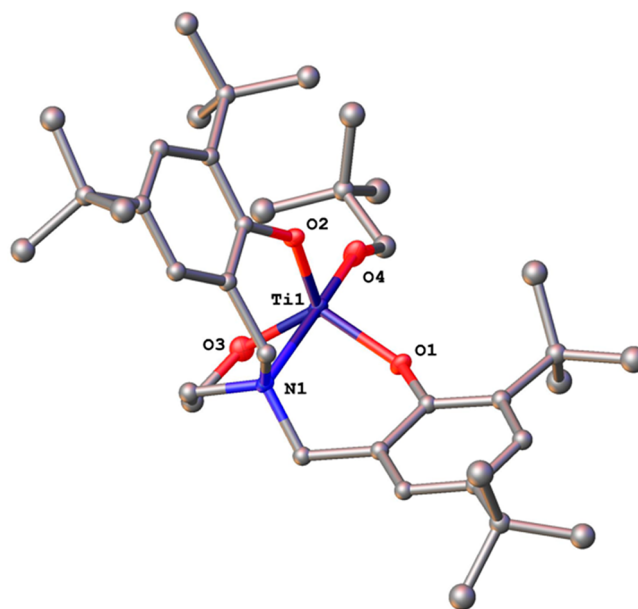


Figure 2. Structure plot of 2. Thermal ellipsoids of heavy atoms drawn at the 30% level with carbon atoms drawn as ball and stick, and H atoms are not shown for clarity. See Supporting Information Table S1 for structural data collection parameters.

N was also noted: N(1)---H(1) = 2.583 Å; O(1)---H(1)---N(1) = 128.2°; N(2)---H(5) = 2.664 Å; O(5)---H(5)---N(2) = 116.9°. Each N atom also strongly H-bonds to the remaining O_{OAr} atom (O_{OAr}---H---N, N(1)---H(2) = 1.927 Å; N(2)---H(4) = 1.959 Å), which results in an elongation of the O_{OAr}---H---O_{EtOH} (O(1)---H(1)---O(3) = 156.984° and O(5)---H(5)---O(6) = 157.933°) and O_{OAr}---H---N (O(2)---H(2)---N(1) = 146.9°; O(4)---H(4)---N(2) = 147.8°). There does not appear to be an intermolecular interaction. Full data collection parameters are available in the Supporting Information. Additionally, ¹H and ¹³C NMR spectra were collected on 1, and the resulting spectral data were in full agreement with the proposed and crystal structure obtained.

1:1 Metal Alkoxide/AM-DBP₂ Compounds. With this well characterized ligand in hand, the initial experiments undertaken were to generate the previously isolated 1:1 [(OR)Ti(AM-DBP₂)] compounds³¹ where OR = OPr^{*i*}, OBU^{*t*} for use as a precursor for nanoceramic materials. Upon mixing of the white ligand with the clear [Ti(OR)₄], the reaction mixture turned an orange-yellow color. No precipitates were

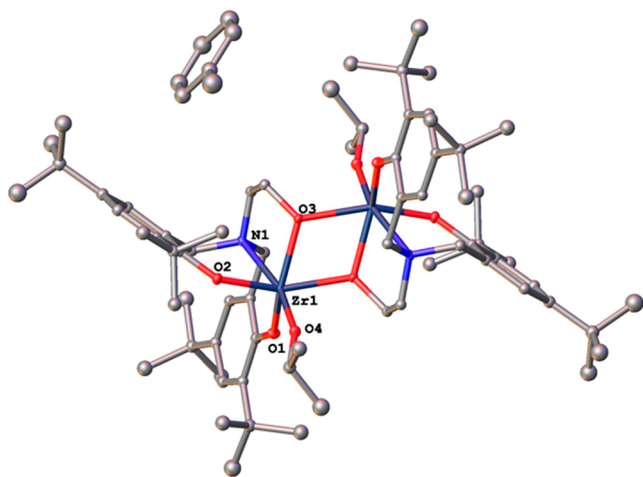


Figure 3. Structure plot of 3-tol. Thermal ellipsoids of heavy atoms drawn at the 30% level with carbon atoms drawn as ball and stick, and H atoms are not shown for clarity. See Supporting Information Table S1 for structural data collection parameters.

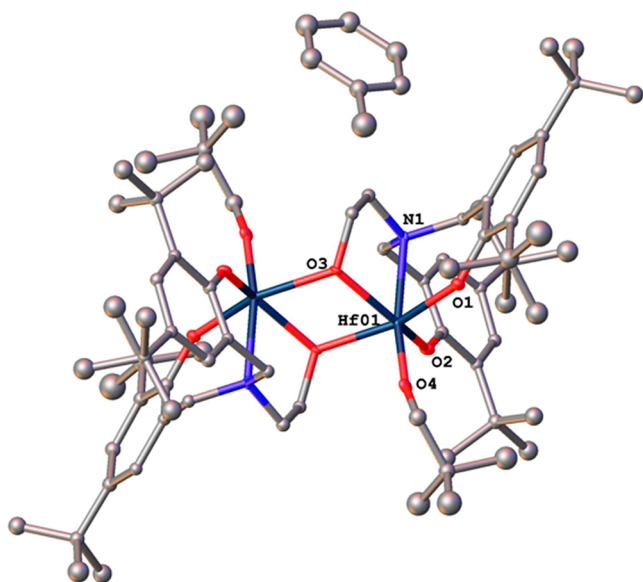


Figure 4. Structure plot of 7-tol. Thermal ellipsoids of heavy atoms drawn at the 30% level with carbon atoms drawn as ball and stick, and H atoms are not shown for clarity. See Supporting Information Table S1 for structural data collection parameters.

observed when the solution sat overnight. Crystals were grown by slow evaporation, and single crystal X-ray experiments were undertaken. In agreement with the literature structure reports, a distorted *TBPY-5* monomer was solved as $[(\text{OBu}^t)\text{Ti}(k^3(\text{O}',\text{O}'',\text{N})\text{AM-DBP}_2)]$ where $\text{OR} = \text{OPr}^i$ and OBu^t .³¹ Since altering the pendant chains on the aryloxy ring from *tert*-butyl to methyl groups led to the formation of the dinuclear $[(\text{OR})\text{Ti}(\mu\text{-(O)})(k^3(\text{O}',\text{O}'',\text{N})\text{AM-DMP}_2)_2]$,^{31,59} it was of interest to determine if the OR ligand could be used to tune the structure as well. This was investigated by introducing the ONep ligand; however, the isolation of **2** (see Figure 2) resulted in the same *TBPY-5* monomeric species, which indicates the parent OR has little impact on the overall structure. The N(1) of the AM-DBP₂ and the O(4) of the ONep ligand were located in the axial position of the Ti metal centers coordination.

It was expected that the larger Zr cation would yield alternative species (i.e., solvates or dinuclear complexes). Upon mixing of the H₃-AM-DBP₂ ligand with the different $[\text{Zr}(\text{OR})_4]$ derivatives in a 1:1 stoichiometry, no color change or precipitate was noted after stirring for 12 h. Crystals were grown by slow evaporation from toluene, and the product proved to be a dinuclear species with each AM-DBP₂ ligand binding to the Zr atoms in a tetradentate manner (*O, O', O'', N*). For these species, the oxygen atom of the ethoxide moiety acts as a bridge between the two metals. The Zr metal finishes its distorted-octahedral (*OC-6*) geometry by retaining the parent OR ligand (OPr^i (**3**); see Figure 3, OBu^t (**4**), ONep (**5**)). Similar reactions were undertaken for $[\text{Hf}(\text{OR})_4]$ species. Again, no color change was noted upon complexation of the AM-DBP₂. The Hf derivatives $[\text{OBu}^t$ (**6**) and ONep (**7**; Figure 4)] were found to adopt similar structures as noted for Zr complexes **3–5**. The general arrangement of **3–7** are in agreement with $[(\text{OR})\text{Ti}(\mu\text{-(O)})(k^3(\text{O}',\text{O}'',\text{N})\text{AM-DMP}_2)_2]$.^{31,59} All attempts to produce the simple monomeric species with the larger metals⁵⁶ were not successful. Scheme 1 shows the two general structure types noted from eq 1.

Metrical Data. Select averaged distance and angles of **2–7** were tabulated in Table 1. In contrast to what was reported for the $[(\text{OR})\text{Ti}(k^4(\text{O},\text{O}',\text{O}'',\text{N})\text{AM-DBP}_2)]$ where $\text{R} = \text{OPr}^i$ or OBu^t ³¹ compounds, the angles around the Ti of **2** proved to adopt a fairly regular *TBPY-5* geometry ($\tau = 0.981$). The bond distances of **2** were found to be in general agreement with the other similarly constructed species.^{31,54–60}

Since no AM-DBP₂ or AM-DMP₂ of Zr or Hf complexes have been previously reported, alternative structural models needed to be used for metrical comparison. While the general constructs of the AM-DBP₂ ligand bound to a Zr were available, none of the ligands possessed the three OH groups but instead had either a (i) fur-2-ylmethyl (*(N,N*-bis(3,5-di-*t*-butyl-2-oxybenzyl)-*N*-((tetrahydrofur-2-yl)methyl)amine-*N,O,O',O''*)),⁵⁴ (ii) tetrahydrofur-2-yl (*(N*-((fur-2-ylmethyl)-*N,N*-bis(3,5-di-*t*-butyl-2-oxybenzyl)amine-*N,O,O',O''*)),⁵⁵ or (iii) methoxy (*(N,N*-bis(3,5-di-*t*-butyl-2-oxybenzyl)-2-methoxyethylamine-*N,O,O',O''*)⁵⁷ group replacing the ethanol tail forming $[(\text{L})\text{Zr}(\text{CH}_2\text{Ph})_2]$ complexes. Only the methoxy derivative (*(N,N*-bis(3,5-di-*t*-butyl-2-oxybenzyl)-2-methoxyethylamine-*N,O,O',O''*) $\text{Hf}(\text{CH}_2\text{Ph})_2$ ⁵⁷ was available for the Hf metrical model. These were used for comparison, along with the dinuclear Ti complex, $[(\text{OR})\text{Ti}(\mu\text{-(O)})(k^3(\text{O}',\text{O}'',\text{N})\text{AM-DMP}_2)_2]$ ^{31,59} whose metrical data was adjusted for the cation size.⁶¹ Initial comparisons between **3** and **7** found the metrical data to be fairly regular, which is expected as Zr and Hf have similar cation sizes in the 4⁺ oxidation state (see Table 1): $\text{M}\cdots\text{M}$ from 3.56–3.61 Å; $\text{M}\cdots\text{N}$ from 2.39–2.54 Å; $\text{M}\cdots\text{O}$ from 1.99–2.00 Å; and $\text{M}\cdots\text{OR}$ from 1.91–1.93 Å. As can be noted in Table 1, the angles around the metal clearly show the distortion from rigorous *OC-6* geometry.

The structures from the DFT simulations were compared with the experimental data of **2–7** (see Table 1). All coordination structures around M noted in the experimental results were found to be stable in the DFT simulations. For the $\text{M}\text{--}\text{O}$ and $\text{M}\text{--}\text{N}$ bonds, the DFT simulations slightly underestimate the bond length by ~1–2% (or 0.02–0.05 Å), which is most notable in the $\text{M}\text{--}\text{OR}$ and $\text{M}\text{--}\text{N}$ bonds. The $\text{M}\cdots\text{M}$ interactions can be difficult to model, but surprisingly these interatomic distances were only 0.03–0.07 Å shorter than in the crystal structures and similar to the variance observed in previous studies of metal oxide clusters.⁶²

Interatomic angles experienced similar variances ($\sim 1\%$ or less). In general, the regularity in the metrical data between the experimental and simulation data indicates the low energy stable molecular structures developed would be useful for additional calculations (*vide infra*).

Bulk Powder Characterization. In an effort to determine if the bulk materials were consistent with the single crystal structures, additional analytical studies were performed. These included FTIR spectroscopy, UV–vis absorbance spectroscopy, and elemental analysis.

FTIR spectroscopy is often a useful means of determining the completion of the alcoholysis reaction through loss of the HO–stretch (3392 cm^{-1}) coupled with the ingrowth of the alkyl groups of the AM-DBP₂ ligand. For 2–7, there was no HO–stretch recorded in the FTIR spectra. Additionally, the stretches assigned to the Bu^t (2954 cm^{-1}) of the H₃-AM-DBP₂ were present (2, 2953; 3, 2964; 4, 2962; 5, 2955; 6, 2954; 7, 2952 cm^{-1}) along with other H₃-AM-DBP₂ alkyl stretches (1481 cm^{-1} : 2, 1478; 3, 1477; 4, 1479; 5, 1479; 6, 1477; 7, 1479 cm^{-1}). The bands observed for 2–7 were much broader than the free ligand with a shoulder peak around 1442 cm^{-1} , which was attributed to the binding of the AM-DBP₂ ligand to the various metal centers. Because of the multiple bends and stretches present in the remainder of the spectra, identification of other stretches associated with the AM-DBP₂ ligand is difficult; however, for each sample, a new M–O stretch was observed for Ti–O ($[(\text{OBu}^t)\text{Ti}(\text{AM-DBP}_2)]^{31}$ and 2 at 610 cm^{-1}), Zr–O (3, 551; 4, 548; 5, 545 cm^{-1}), and Hf–O (6, 545; 7, 543 cm^{-1}).⁶³ These data indicate that the general features of the AM-DBP₂, pendant OR, and M–O bonds are present.

Elemental analyses of the majority of compounds were found to be in agreement with the solid-state structures, in terms of the percent composition. For 5 and 7, the %C was too low but may be a reflection of the ONep ligand, which is often reported to not have reproducible thermal elemental analyses.^{28,29} For 5, when the $-\text{CH}_2\text{C}(\text{CH}_3)_3$ moieties are removed from consideration, the calculated values of 5 are in agreement with experimental values. Attempts at employing mass spectral analysis were not informative in terms of identifying the parent ions. In particular, the main peaks found were not associated with any aspect of the observed structures. This may be due to the sensitivity of the remaining alkoxide ligand reacting with ambient atmospheric water, prior to analysis.

As noted, the solid-state structures of 2–7 were determined by single crystal X-ray diffraction studies as both monomeric and dimeric complexes. If the solid state symmetry was retained upon dissolution, the ¹H NMR spectra of these compounds were expected to yield the following resonances: two singlets for the aromatic protons, two resonances for the *t*-butyl aryl (OAr–Bu^t) substituents, the appropriate resonances for the alkoxides (singlet for Bu^t; two singlets for ONep), and three methylene resonances (benzyl hydrogens, O–CH₂ and CH₂–N). A variety of solvent systems were explored (toluene-*d*₈, THF-*d*₈, pyridine-*d*₈) in an attempt to determine the solution behavior of 2–7. Unfortunately, these spectra were dominated by numerous, overlapping, broad resonances that could not be meaningfully interpreted. In contrast, ¹H NMR spectra collected for 2–7 in CDCl₃ (Sigma-Aldrich, 99.8 atom % D; see the Supporting Information for the full spectra obtained in CDCl₃) revealed the appropriate resonances for the OAr–Bu^t and the parent OR; however, the various

methylene resonances were broad, “missing”, or the integration on the observed peaks proved to be inconsistent with the structural properties. This was believed to be due to fluxional and/or monomer–dimer exchange in solution 2–7 in CDCl₃.

Therefore, variable temperature ¹H NMR studies were undertaken to further clarify the behavior of these compounds in solution. Initial efforts to lock out a single structure by low temperature NMR experiments failed due to preferential crystallization of the precursors out of solution. Alternatively, high temperature spectra in CDCl₃ were collected with the expectation that monomeric species would be favored at elevated temperatures. The high temperature variable temperature NMR studies are shown in the Supporting Information. While there were significant changes noted, in the general spectra of 2–7, a mixture of monomers and dimers was still present for each sample. Unfortunately, the higher temperatures necessary to force complete conversion to the monomeric form was not possible as the CDCl₃ temperature limit had been reached. Additional experiments to elucidate the solution behavior of 2–7 were not undertaken.

Since some of the M-(AM-DBP₂) derivatives were highly colored, UV–vis absorbance spectroscopic analyses were undertaken to further assist in characterizing 2–7. The H₃-AM-DBP₂ ligand was found to have a strong absorbance at 293 nm, which was preliminarily assigned to a $\pi \rightarrow \pi^*$ transition. A similar absorbance was noted for the various derivatives with λ_{max} for $[(\text{OBu}^t)\text{Ti}(\text{AM-DBP}_2)]$ at 285; 2, 290; 3, 298; 4, 294; 5, 294; 6, 293; 7, 293 nm. In addition, another peak was readily observed for the Ti derivatives ($\lambda_{\text{max}} = 330\text{ nm}$ for OBu^t, and 340 nm for 2). There is a minor λ_{max} noted for the Zr (3, 352; 4, 384; and 5, 354 nm) and the Hf (6, 373 and 7, 355 nm) compounds. On the basis of the quality of the DFT models, TD-DFT UV–vis absorbance calculations were undertaken to assist in assigning the absorbances noted experimentally. In the Ti derivative 2, the calculated spectrum revealed a major absorbance at 270 nm with a significant shoulder at 341 nm. This is consistent with the two absorbances noted in the experimental spectrum of 2. The shoulder at 341 nm in the UV–vis absorbance spectrum of 2 is attributed to a mixed $\pi \rightarrow \pi^*$ and ligand to metal charge transfer (LMCT) transitions (from visualization of the molecular orbitals shown in Figure S15). The LMCT transition is largely in the AM-DBP₂ phenyl ring and Ti–O and the $\pi \rightarrow \pi^*$ in the C–C π bonds (HOMO and HOMO-1 molecular orbitals) which transition to π^* bonds (LUMO and LUMO+1 molecular orbitals). The shoulder in 3 develops from a LMCT transition between the AM-DBP₂ and the associated Ti atom and ligand linkages. Structurally, the Ti-based molecule 2 has a shorter M–O_{AM-DBP₂}, M–O_{Am-EtO}, and M– μ -OR interatomic distance (Table 1) than 3, 4, 5, 6, and 7. A strong Ti–O interaction may be playing a role in the development of the intense shoulder in the UV–vis absorbance spectra.

Between compounds 2–7, the variance in λ_{max} values arise from shifts in the HOMO \rightarrow LUMO, HOMO–1 \rightarrow LUMO +1, and HOMO–1 \rightarrow LUMO transitions (Table 2). The model spectra for the Zr compounds (3, 4, and 5) identified a primary peak for each, which was within 10 nm of the value of the single peak experimentally observed. The λ_{max} noted for the Hf-based molecules' spectra (6, 7) revealed a consistent blue-shift of 30–40 nm from the experimental values. This variation was assumed to be a function of the selected DFT methods and complications with modeling the *f*-electrons. The

absorbance maxima for 3–6 were determined to arise primarily from HOMO → LUMO, HOMO–1 → LUMO+1, and HOMO–1 → LUMO transitions, as shown in Table 2. Overall, the transitions in the Ti-based molecule 2 was found to be shifted to much higher wavelengths than in the Zr- and Hf-based molecules. This may be a reflection of the final structure types.

Nanomaterials. In order to determine the influence, the AM-DBP₂ had on the final nanomaterials generated, a series of SOLVO reactions were undertaken using both the parent alkoxides [M(ONep)₄]₂ (M = Ti, Zr, and Hf) and compounds 2, 5, and 7 under similar conditions. The latter compounds were selected since they had the ONep ligand and the AM-DBP₂ modifier, which allows for a meaningful comparison of the final materials.

The TGA spectra (see Supporting Information) were collected for the parent alkoxide and 2, 5, and 7 to determine if they would be acceptable for nanomaterial production by solution routes. The parent alkoxides all showed early low temperature decomposition, with final weight losses completed by 300 °C. In contrast, the spectra for the AM-DBP₂ species had much higher final weight loss temperatures, 500 °C with the initiation of these weight losses below 300 °C. Therefore, the decomposition pathways of the AM-DBP₂ derivatives versus the parent alkoxides were expected to vary significantly upon processing.

Of the solution routes available, SOLVO processing was selected using octadecene due to the high boiling point, non-coordinating nature, low toxicity, and low water content. The reactions and powder isolated were run under inert atmospheres, as described in the Experimental Section, to eliminate potential hydrolysis products. After this, a comparison of the materials generated was undertaken using PXRD, TEM (Figure 5), and DLS (Figure 6). For each sample isolated, an amorphous material was generated, as confirmed by PXRD analyses. A subset of these samples was fired (650 °C; 1/2 h) to crystallize the powders. Samples were analyzed by PXRD and proved to be the MO₂ (TiO₂: PDF 99-000-3236 (rutile)/98-000-0081 (anatase) (2); ZrO₂: PDF 01-072-2742 (3), 01-075-9645 (4), 01-072-2742 (5); HfO₂: PDF 00-043-1017(6), 00-053-0560 (7)). The spectra for all of the samples are shown in the Supporting Information.

TEM images were collected on all of the samples and are shown in Figure 5. For the [Ti(ONep)₄], there are flat round plate-shaped particles on the order of 30–40 nm in size (Figure 5a,i) but also smaller species distributed throughout the sample. For 2, the particles were also identified as flat plates (Figure 5a,ii) but appear to be smaller in size ranging from 10–20 nm in size, with little evidence of smaller particulates present. The [Zr(ONep)₄] generated powders were found to be small particulates (Figure 5b,i), ~1 nm in size. In contrast, the particles isolated from 5 reveal larger particles formed in the range of 5–20 nm; however, it is of note that a number of the smaller particles were present (Figure 5b,ii). The Hf system (Figure 5c) shows a similar trend with small particles observed for the parent [Hf(ONep)₄] but much larger particles (20–40 nm) for 7. Combined, these data demonstrate that the AM-DBP₂ plays a role in altering the particulate size, most likely by introducing controlled hydrolysis regions.

Additional classification of the particulate size was undertaken to verify the trends identified in the TEM images. The PSD results determined from the DLS analyses are shown in

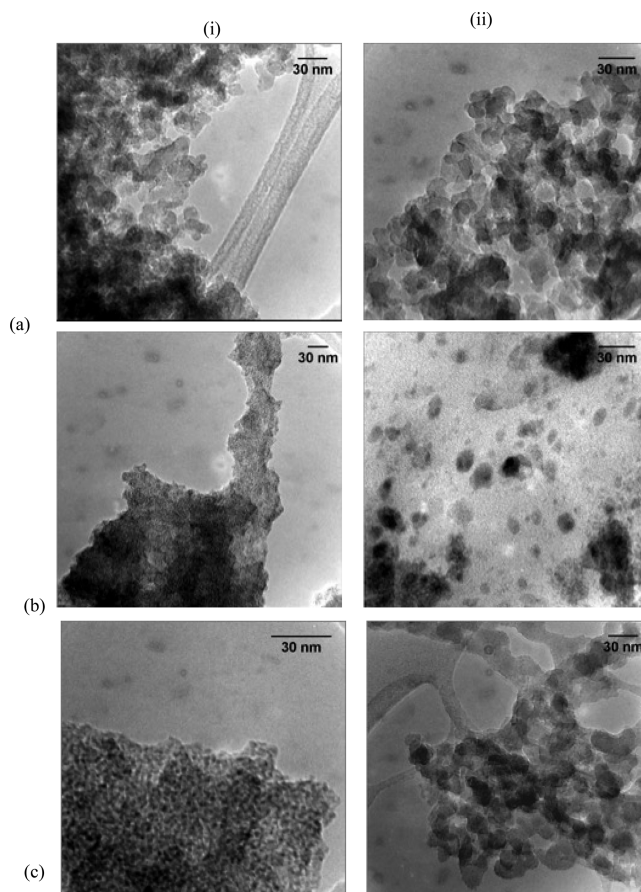


Figure 5. TEM images for column (i) [M(ONep)₄] and column (ii) [(AM-DBP₂)M(ONep)_n] where M = (a) Ti and 2, (b) Zr and 5, and (c) Hf and 7.

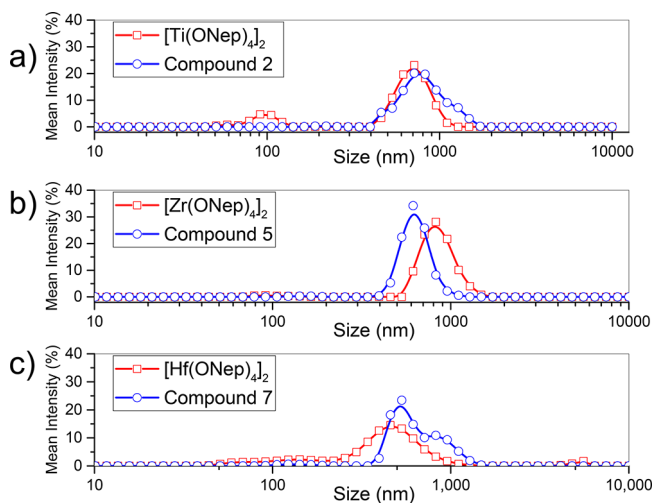


Figure 6. DLS data for nanomaterials generated from [M(ONep)₄] and [(AM-DBP₂)M(ONep)_n] where M = (a) Ti and 2, (b) Zr and 5, and (c) Hf and 7.

Figure 6. The ceramic material generated from the parent [Ti(ONep)₄] was found to possess a bimodal distribution, with peaks centered at 713 (84%) and 91 nm (15%). In contrast, the particles generated from 2 were monomodal with a cluster size of 834 nm (99%). For [Zr(ONep)₄], there was also a bimodal distribution, with peaks at 862 (98%) and 34 nm (2%), but 5 had a primary peak at 641 nm (99%) with a

very small secondary cluster (less than 1%). For $[\text{Hf}(\text{ONep})_4]$, a very broad PSD was recorded, with the main peak at 497 nm (81%), and additional peaks noted at 732 (14%) and 1353 nm (1.2%). In contrast, compound 7 has a much tighter distribution at 697 (97%) nm with a small fraction of nanomaterials at 46 nm (3%). These results indicate the colloidal stability of the product and their aggregation into larger polycrystals. The DLS data also show the peak locations (i.e., size) and intensity value (i.e., particle frequency/number/volume) for the generated particle distribution. The distribution of particle sizes relates to the precursor decomposition in solution, as well as their state of agglomeration during the SOLVO process. Since the SOLVO experiments were conducted without stirring, there is an inherent inhomogeneity in the reaction mixture due to sedimentation and cluster growth, which makes interpretation of the data difficult. Nonetheless, a generalized understanding can be drawn from the location and width of the measured peaks. Sol–gel reaction theory describes how the decomposition of the precursor leads to polymerize or crystallize the metal oxide, which is then followed by particulate growth. Consequently, the rapid decomposition of a precursor leads to numerous discrete growth nuclei, yielding small particles, whereas slow decomposition leads to deliberate nucleation and growth processes that result in particle aggregation and larger, broader particle populations. The size (nm) of the predominant DLS peak is therefore a proxy for the rate of reaction - rapid reaction forming nanomaterials and slow precursor decomposition followed by growth or aggregation giving a broad peak distribution.

For the parent $[\text{M}(\text{ONep})_4]$ precursors' SOLVO products, there is a general trend toward bimodal or multimodal distributions. Each sample reveals the presence of a broad predominant peak in the submicron range along with measurable amounts of nanomaterials. This type of distribution may result if the initial particles that form are large and subsequently precipitate. The remaining soluble precursors continue to decompose but under diluted conditions, providing the source of the nanoparticles. This suggests that the cluster formation occurs via particle agglomeration, and the nanoparticles form by dilute nucleation over time. The TEM images in Figure 5 confirm the heterogeneous nucleation growth, revealing polycrystalline products or polycrystalline materials in an amorphous matrix. The major size populations were fit with Gaussian peaks in each case, whereas the nanoparticle presence is very small. With larger size as a proxy for slower reactivity, the ONep compounds indicate that the rate of nucleation from $[\text{M}(\text{ONep})_4]$ is $\text{Zr} > \text{Ti} > \text{Hf}$. While the particle distribution of the AM-DBP₂ precursors 2 and 7 has a bimodal character, the most intense peak in size is larger than that of the respective $[\text{M}(\text{OR})_4]$. For each of these samples, there is an additional shoulder in the distribution, above the major peak, which suggests that the decomposition reaction of the compound is slowed kinetically compared to the $[\text{M}(\text{OR})_4]$. This change is attributed to the stability induced by the tetradentate AM-DBP₂ modifier. This is consistent with the TGA/DSC curves and the larger particles noted in the TEM data. However, for compound 5 the PSD shows formation of a lower particle size entirely and no shoulder at higher peak size. The TEM images indicate that a very diverse set of materials were generated, which complicates the understanding of the precursor/material relationship. It is of note that while more studies are necessary to fully elucidate

the growth mechanism of these particles and how the stabilized AM-DBP₂ compounds impact this process and the morphology of the final nanomaterials produced.

SUMMARY AND CONCLUSIONS

The modification of group 4 metal alkoxides with the AM-DBP₂ ligand was found to produce two types of structures depending on the cation, which were identified as $[(\text{OR})\text{Ti}(k^4(\text{O},\text{O}',\text{O}'',\text{N}))-AM\text{-DBP}_2]$ (2) and $[(\text{OR})\text{M}(\mu(\text{O})-k^3(\text{O}',\text{O}'',\text{N}))-AM\text{-DBP}_2)_2]$ (3–7). In all instances, the bonding mode of the AM-DBP₂ ligand was found by single crystal X-ray diffraction experiments to adopt a tetradentate binding mode, using the three O atoms and the N to chelate to the metal. The introduction of this ligand substantially increased the thermal stability in comparison to the parent alkoxides as determined by TGA analyses. DFT calculations were found to generate useful metrical models which were applied to elucidate the various UV–vis absorbance spectra. The thermal stability led to larger and more uniform particles of the AM-DBP₂ precursors in comparison to their parent alkoxides when SOLVO routes were employed. The changes wrought by the AM-DBP₂ precursors are anticipated to allow for better N-ink formulations due to the slightly larger size and uniformity of sample. Further attempts to tailor the size of the nanomaterials for N-ink applications using different processing and solution preparations are underway.

ASSOCIATED CONTENT

Supporting Information

The Supporting Information is available free of charge on the ACS Publications website at DOI: 10.1021/acs.inorgchem.8b01907.

Data collection parameters for 1–7; structure plots of 1–7; UV–vis absorbance spectra of 2–7, and H3-AM-DBP₂; TGA/DSC, and DLS data: parent alkoxides, 2, 5, and 7 (PDF)

Accession Codes

CCDC 1854168–1854174 contain the supplementary crystallographic data for this paper. These data can be obtained free of charge via www.ccdc.cam.ac.uk/data_request/cif, or by emailing data_request@ccdc.cam.ac.uk, or by contacting The Cambridge Crystallographic Data Centre, 12 Union Road, Cambridge CB2 1EZ, UK; fax: +44 1223 336033.

AUTHOR INFORMATION

Corresponding Author

*E-mail: tjboyle@Sandia.gov. Phone: (505)272-7625. Fax: (505)272-7336.

ORCID

Timothy J. Boyle: 0000-0002-1251-5592

Present Addresses

#(D.T.Y.) North Carolina State University, Department of Chemistry, 2620 Yarbrough Drive, Raleigh, NC 27695-8204.

†(C.J.A.) Northwestern University, Department of Chemistry, 2504 Silverman Hall, 2170 Campus Dr., Evanston, IL 60208.

‡(M.T.B.) University of Wisconsin–Madison, Department of Chemistry, 1101 University Avenue, Madison, Wisconsin 53706.

Notes

The authors declare no competing financial interest.

ACKNOWLEDGMENTS

This work was supported by the NSF REU program at UNM (Grant Number CBET-1560058 and DMR 1263387), as well as the Laboratory Directed Research and Development program at Sandia National Laboratories. Sandia National Laboratories is a multimission laboratory managed and operated by National Technology and Engineering Solutions of Sandia, LLC., a wholly owned subsidiary of Honeywell International, Inc., for the U.S. Department of Energy's National Nuclear Security Administration under contract DE-NA0003525.

REFERENCES

- (1) Lui, H.; Webster, T. J. Mechanical properties of dispersed ceramic nanoparticles in polymer composites for orthopedic applications. *Int. J. Nanomed.* **2010**, *5*, 299–313.
- (2) Yang, L.; Sheldon, B. W.; Webster, T. J. Nanophase ceramics for improved drug delivery: Current opportunities and challenges. *Am. Ceram. Soc. Bull.* **2010**, *89*, 24–32.
- (3) Fujishima, A.; Rao, T. N.; Tryk, D. A. Titanium dioxide photocatalysis. *J. Photochem. Photobiol., C* **2000**, *1*, 1–21.
- (4) Aflaki, M.; Davar, F. Synthesis, luminescence, and photocatalyst properties of zirconia nanosheets by modified Pechini method. *J. Mol. Liq.* **2016**, *221*, 1071–1079.
- (5) Schmidt, W. R.; Campbell-Hugener, T.; Bhatia, T. Siloxane removal via silicate formation for lifetime extension of photocatalytic devices. US 20100120610 A1, 2010.
- (6) Bullock, D. E.; Rosenberg, S. E.; Comeaux, C. M. A thermal management system for high temperature events. WO 2006074449 A2, 2006.
- (7) Hepburn, S. P. Fibrous materials. US 3996145 A, 1976.
- (8) Ou, D. L.; White, S. O. Aerogel composites with complex geometries. US 20100080949 A1, 2010.
- (9) Bryan, P. S.; Lambert, P. M.; Towers, C. M.; Jarrold, G. S. X-ray intensifying screen including a titanium activated hafnium dioxide phosphor containing erbium to reduce afterglow. US 4972086 A, 1990.
- (10) AZO nano Zirconium oxide nanoparticles – Properties, applications. <http://www.azonano.com/article.aspx?ArticleID=3347>. Last accessed Oct 2017.
- (11) Fiorentini, V.; Gulleri, G. Theoretical evaluation of zirconia and hafnia as gate oxides for Si microelectronics. *Phys. Rev. Lett.* **2002**, *89*, 266101:1–4.
- (12) Zheng, J. X.; Ceder, G.; Maxisch, T.; Chim, W. K.; Choi, W. K. First-principles study of native point defects in hafnia and zirconia. *Phys. Rev. B: Condens. Matter Mater. Phys.* **2007**, *75*, 104112:1–7.
- (13) Hausmann, D. M.; Kim, E.; Becker, J.; Gordon, R. G. Atomic layer deposition of hafnium and zirconium oxides using metal amide precursors. *Chem. Mater.* **2002**, *14*, 4350–4358.
- (14) US Research Nanomaterials Inc. Hafnium oxide nanoparticle (HfO₂, 99.99%, high purity, 61–80 nm, cubic); <http://www.us-nano.com/inc/sdetail/489>. Last accessed Oct 2017.
- (15) Mise, N.; Ogawa, A.; Tonomura, O.; Sekiguchi, T.; Horii, S.; Itatani, H.; Saito, T.; Sakai, M.; Takebayashi, Y.; Yamazaki, H.; Torii, K. Theoretical screening of candidate materials for DRAM capacitors and experimental demonstration of a cubic-hafnia MIM capacitor. *IEEE Trans. Electron Devices* **2010**, *57*, 2080–2086.
- (16) Lewis, J. A.; Gratson, G. M. Direct writing in 3 dimensions. *Mater. Today* **2004**, *7*, 32–39.
- (17) Wu, S.-Y.; Yang, C.; Hsu, W.; Lin, L. 3D-printed microelectronics for integrated circuitry and passive wireless sensors. *Microsystem & Nanoengineering* **2015**, *1*, 15013:1–9.
- (18) Sarobol, P.; Cook, A.; Clem, P. G.; Keicher, D.; Hirschfeld, D.; Hall, A. C.; Bell, N. S. Additive manufacturing of hybrid circuits. *Annu. Rev. Mater. Res.* **2016**, *46*, 41–62.
- (19) Lu, W. S.; Schmidt, H. Synthesis of nanosized BaSnO₃ powders from metal isopropoxides. *J. Sol-Gel Sci. Technol.* **2007**, *42*, 55–64.
- (20) Niederberger, M.; Garnweitner, G.; Buha, J.; Polleux, J.; Ba, J. H.; Pinna, N. Nonaqueous synthesis of metal oxide nanoparticles: Review and indium oxide as case study for the dependence of particle morphology on precursors and solvents. *J. Sol-Gel Sci. Technol.* **2006**, *40*, 259–266.
- (21) Boyle, T. J.; Steele, L. A. M.; Burton, P. D.; Hoppe, S. M.; Lockhart, C.; Rodriguez, M. A. Synthesis and structural characterization of a family of modified hafnium *tert*-butoxide for use as precursors to hafnia nanoparticles. *Inorg. Chem.* **2012**, *51*, 12075–12092.
- (22) Nikonova, O. A.; Nedelec, J. M.; Kessler, V. G.; Seisenbaeva, G. A. Precursor-directed assembly of complex oxide nanobeads: The role of strongly coordinated inorganic anions. *Langmuir* **2011**, *27*, 11622–11628.
- (23) Turova, N. Y.; Turevskaya, E. P.; Kessler, V. G.; Yanovskaya, M. I. *The Chemistry of Metal Alkoxides*; Kluwer Academic Publishers: Boston, 2002.
- (24) Boyle, T. J.; Schwartz, R. W.; Doedens, R. J.; Ziller, J. W. Synthesis and structure of novel group IV tridentate alkoxide complexes and ceramic thin films derived therefrom. X-ray structures of (H₃CC(CH₂-μ₃-O)(CH₂-μ₃-O)₂)₂Ti₄(OCH(CH₃)₂)₁₀, (H₃CCH₂C(CH₂-μ₃-O)(CH₂-μ-O)₂)₂Ti₄(OCH(CH₃)₂)₁₀, and (H₃CC(CH₂-μ-O)₃)₂Zr₄(μ-OCH(CH₃)₂)₂(OCH(CH₃)₂)₈. *Inorg. Chem.* **1995**, *34*, 1110–1120.
- (25) Caulton, K. G.; Hubert-Pfalzgraf, L. G. Synthesis, structural principles, and reactivity of heterometallic alkoxides. *Chem. Rev.* **1990**, *90*, 969–995.
- (26) Safaei, E.; Rasouli, M.; Weyhermueller, T.; Bill, E. Synthesis and characterization of binuclear [ONXO]-type amine-bis(phenolate) copper(II) complexes. *Inorg. Chim. Acta* **2011**, *375*, 158–165.
- (27) Higham, C. S.; Dowling, D. P.; Shaw, J. L.; Cetin, A.; Ziegler, C. J.; Farrell, J. R. Multidentate aminophenol ligands prepared with Mannich condensations. *Tetrahedron Lett.* **2006**, *47*, 4419–4423.
- (28) Boyle, T. J.; Alam, T. M.; Mechenbier, E. R.; Scott, B. L.; Ziller, J. W. Titanium(IV) neopentoxides. X-ray structures of Ti₃(μ₃-Cl)(μ-OCH₂CMe₃)₃(OCH₂CMe₃)₆ and [Ti(μ-OCH₂CMe₃)-(OCH₂CMe₃)₃]₂. *Inorg. Chem.* **1997**, *36*, 3293–3300.
- (29) Boyle, T. J.; Ottley, L. A. M.; Hoppe, S. M.; Campana, C. F. Series of comparable dinuclear group 4 neo-pentoxide precursors for production of pH dependent group 4 nanoceramic morphologies. *Inorg. Chem.* **2010**, *49*, 10798–10808.
- (30) Siegl, W. O.; Chattha, M. S. Eur. Patent Application, 276073, 1988.
- (31) Padmanabhan, S.; Katao, S.; Nomura, K. Synthesis and Structure of Titanatranes Containing Tetradentate Trianionic Donor Ligands of the Type [(O-2,4-R₂C₆H₂-6-CH₂)₂(OCH₂CH₂)]N₃- and Their Use in Catalysis for Ethylene Polymerization. *Organometallics* **2007**, *26*, 1616–1626.
- (32) Sheldrick, G. M. Crystal Structure Refinement with SHELXL. *Acta Crystallogr., Sect. C: Struct. Chem.* **2015**, *71*, 3–8.
- (33) Sheldrick, G. M. A. Short History of SHELX. *Acta Crystallogr., Sect. A: Found. Crystallogr.* **2008**, *64*, 112–122.
- (34) *The Saint, SADABS, Apex3 Package*; Bruker AXS: Madison, WI, 2012.
- (35) Dolomanov, O. V.; Bourhis, L. J.; Gildea, R. J.; Howard, J. A. K.; Puschmann, H. OLEX2: A Complete Structure Solution, Refinement and Analysis Program. *J. Appl. Crystallogr.* **2009**, *42*, 339–341.
- (36) Groom, C. R.; Bruno, I. J.; Lightfoot, M. P.; Ward, S. C. The Cambridge Structural Database. *Acta Crystallogr., Sect. B: Struct. Sci., Cryst. Eng. Mater.* **2016**, *72*, 171–179.
- (37) Frisch, M. J.; Trucks, G. W.; Schlegel, H. B.; Scuseria, G. E.; Robb, M. A.; Cheeseman, J. R.; Scalmani, G.; Barone, V.; Mennucci, B.; Petersson, G. A.; Nakatsuji, H.; Caricato, M.; Li, X.; Hratchian, H. P.; Izmaylov, A. F.; Bloino, J.; Zheng, G.; Sonnenberg, J. L.; Hada, M.; Ehara, M.; Toyota, K.; Fukuda, R.; Hasegawa, J.; Ishida, M.; Nakajima, T.; Honda, Y.; Kitao, O.; Nakai, H.; Vreven, T.; Montgomery, J. A., Jr.; Peralta, J. E.; Ogliaro, F.; Bearpark, M.; Heyd, J. J.; Brothers, E.; Kudin, K. N.; Staroverov, V. N.; Kobayashi,

- R.; Normand, J.; Raghavachari, K.; Rendell, A.; Burant, J. C.; Iyengar, S. S.; Tomasi, J.; Cossi, M.; Rega, N.; Millam, J. M.; Klene, M.; Knox, J. E.; Cross, J. B.; Bakken, V.; Adamo, C.; Jaramillo, J.; Gomperts, R.; Stratmann, R. E.; Yazyev, O.; Austin, A. J.; Cammi, R.; Pomelli, C.; Ochterski, J. W.; Martin, R. L.; Morokuma, K.; Zakrzewski, V. G.; Voth, G. A.; Salvador, P.; Dannenberg, J. J.; Dapprich, S.; Daniels, A. D.; Farkas, O.; Foresman, J. B.; Ortiz, J. V.; Cioslowski, J.; Fox, D. J. *Gaussian 09*; Gaussian, Inc.: Wallingford, CT, USA, 2009.
- (38) Francl, M. M.; Pietro, W. J.; Hehre, W. J.; Binkley, J. S.; Gordon, M. S.; DeFrees, D. J.; Pople, J. A. Self-consistent molecular orbital methods. XXIII. A polarization-type basis set for second-row elements. *J. Chem. Phys.* **1982**, *77*, 3654–3665.
- (39) Lee, C.; Yang, W.; Parr, R. G. Development of the Colle-Salvetti correlation-energy formula into a functional of the electron density. *Phys. Rev. B: Condens. Matter Mater. Phys.* **1988**, *37*, 785–789.
- (40) Becke, A. D. A new mixing of Hartree–Fock and local density-functional theories. *J. Chem. Phys.* **1993**, *98*, 1372–1377.
- (41) Hay, P. J.; Wadt, W. R. Ab initio effective core potentials for molecular calculations. Potentials for K to Au including the outermost core orbitals. *J. Chem. Phys.* **1985**, *82*, 299–310.
- (42) Wadt, W. R.; Hay, P. J. Ab initio effective core potentials for molecular calculations. Potentials for main group elements Na to Bi. *J. Chem. Phys.* **1985**, *82*, 284–298.
- (43) Hehre, W. J.; Ditchfield, R.; Pople, J. A. Self-consistent molecular orbital methods. XII. Further extensions of Gaussian-type basis sets for use in molecular orbital studies of organic molecules. *J. Chem. Phys.* **1972**, *56*, 2257–2261.
- (44) Hariharan, P. C.; Pople, J. A. The influence of polarization functions on molecular orbital hydrogenation energies. *Theor. Chim. Acta* **1973**, *28*, 213–222.
- (45) Francl, M. M.; Pietro, W. J.; Hehre, W. J.; Binkley, J. S.; Gordon, M. S.; DeFrees, D. J.; Pople, J. A. Self-consistent molecular orbital methods. XXIII. A polarization-type basis set for second-row elements. *J. Chem. Phys.* **1982**, *77*, 3654–3665.
- (46) Petersson, A.; Bennett, A.; Tensfeldt, T. G.; Al-Laham, M. A.; Shirley, W. A.; Mantzaris, J. A complete basis set model chemistry. I. The total energies of closed-shell atoms and hydrides of the first-row elements. *J. Chem. Phys.* **1988**, *89*, 2193–2218.
- (47) Sabin, J. R.; Varzatskii, O. A.; Voloshin, Y. Z.; Starikova, Z. A.; Novikov, V. V.; Nemykin, V. N. Insight into the electronic structure, optical properties, and redox behavior of the hybrid phthalocyanino-clathrochelates from experimental and density functional theory approaches. *Inorg. Chem.* **2012**, *51*, 8362–8372.
- (48) Boyle, T. J.; Neville, M. L.; Parkes, M. V. Synthesis and characterization of a series of group 4 phenoxy-thiol derivatives. *Polyhedron* **2016**, *110*, 1–13.
- (49) Si, Y.; Yang, G.; Hu, M.; Wang, M. Assignment of the absolute configuration of dinuclear zirconium complexes containing two homochiral N atoms using TDDFT calculations of ECD. *Chem. Phys. Lett.* **2011**, *502*, 266–270.
- (50) Zhang, M.-D.; Zhang, Z.-Y.; Bao, Z.-Q.; Ju, Z.-M.; Wang, X.-Y.; Zheng, H.-G.; Ma, J.; Zhou, X.-F. Promising alkoxy-wrapped porphyrins with novel push–pull moieties for dye-sensitized solar cells. *J. Mater. Chem. A* **2014**, *2*, 14883–14889.
- (51) Stratmann, R. E.; Scuseria, G. E.; Frisch, M. J. An efficient implementation of time-dependent density-functional theory for the calculation of excitation energies of large molecules. *J. Chem. Phys.* **1998**, *109*, 8218–8224.
- (52) Furche, F.; Ahlrichs, R. Adiabatic time-dependent density functional methods for excited state properties. *J. Chem. Phys.* **2002**, *117*, 7433–7447.
- (53) O’Boyle, N. M.; Tenderholt, A. L.; Langner, K. M. CcLib: a library for package-independent computational chemistry algorithms. *J. Comput. Chem.* **2008**, *29*, 839–845.
- (54) Groysman, S.; Goldberg, I.; Kol, M.; Genizi, E.; Goldschmidt, Z. From THF to furan: Activity tuning and mechanistic insight via sidearm donor replacement in group IV amine bis(phenolate) polymerization catalysts. *Organometallics* **2003**, *22*, 3013–3015.
- (55) Groysman, S.; Goldberg, I.; Kol, M.; Genizi, E.; Goldschmidt, Z. Group IV complexes of an amine bis(phenolate) ligand featuring a THF sidearm donor: from highly active to living polymerization catalysts of 1-hexene. *Inorg. Chim. Acta* **2003**, *345*, 137–144.
- (56) Tshuva, E. Y.; Goldberg, I.; Kol, M.; Goldschmidt, Z. Living polymerization and block copolymerization of α -olefins by an amine bis(phenolate) titanium catalyst. *Chem. Commun.* **2001**, 2120–2121.
- (57) Tshuva, E. Y.; Groysman, S.; Goldberg, I.; Kol, M.; Goldschmidt, Z. [ONXO]-Type amine bis(phenolate) zirconium and hafnium complexes as extremely active 1-hexene polymerization catalysts. *Organometallics* **2002**, *21*, 662–670.
- (58) Boyle, T. J.; Yonemoto, D. T.; Steele, L.; Farrell, J.; Renehan, P.; Huhta, T. Coordination Chemistry of N,N,N’,N’-Tetrakis(3,5-substituted benzyl-2-oxide)-2,2(ethylenedioxy)diethanamine Modified Group 4 Metal Alkoxides. *Inorg. Chem.* **2012**, *51*, 12023–12031.
- (59) Gurubasavaraj, P. M.; Nomura, K. Synthesis and structural analysis of titanatranes bearing terminal substituted aryloxo ligands of the type [Ti(OAr){((O-2,4-Me₂C₆H₂-6-CH₂)₂(OCH₂CH₂)N)}]_n ($n = 1, 2$): Effect of aryloxo substituents in the ethylene polymerization. *Inorg. Chem.* **2009**, *48*, 9491–9500.
- (60) Kim, Y.; Verkade, J. G. Novel titanatranes with different ring sizes: Syntheses, structures, and lactide polymerization catalytic capabilities. *Organometallics* **2002**, *21*, 2395–2399.
- (61) Shannon, R. D. Revised effective ionic radii and systematic studies of interatomic distances in halides and chalcogenides. *Acta Crystallogr., Sect. A: Cryst. Phys., Diffr., Theor. Gen. Crystallogr.* **1976**, *32*, 751–767.
- (62) Zhao, Y.-X.; Ding, X.-L.; Ma, Y.-P.; Wang, Z.-C.; He, S.-G. Transition metal oxide clusters with character of oxygen-centered radical: a DFT study. *Theor. Chem. Acc.* **2010**, *127*, 449–465.
- (63) Bradley, D. C.; Mehrotra, R. C.; Gaur, D. P. *Metal Alkoxides*; Academic Press: New York, 1978.